1-1-2019

In situ incorporation of nanostructured antimony in an N-doped carbon matrix for advanced sodium-ion batteries

Zhibin Wu
University of Wollongong, zw120@uowmail.edu.au

Bernt Johannessen
Australian Synchrotron

Wenchao Zhang
University of Wollongong, wz990@uowmail.edu.au

Wei Kong Pang
University of Wollongong, wkpang@uow.edu.au

Jianfeng Mao
University of Wollongong, jmao@uow.edu.au

See next page for additional authors

In situ incorporation of nanostructured antimony in an N-doped carbon matrix for advanced sodium-ion batteries

Abstract

Herein, a facile one-step and solvent-free pyrolysis method was developed to control the synthesis of nanostructured Sb embedded in an N-doped carbon matrix (Sb@G x N y -T, where T, G x and N y denote the annealing temperature and the mass (g) of glucose and NH 4 Cl used in the process, respectively). By adjusting these parameters, hybrid architectures can be in situ constructed, including hollow Sb embedded in holeless carbon matrixes (Sb@G 0.25 N 0.5 -950) and Sb nanoplates embedded in holey carbon matrixes (Sb@G 0.25 N 0.25 -950). Our findings suggest that the formation of diverse nanostructures closely relate to the sublimation and evaporation of Sb, and the structural remold of liquid Sb by surface tension. Benefitting from the unique structural features, these optimized electrodes show highly reversible sodium storage with high specific capacities and good cycling stability. More importantly, this strategy can be further extended to other material systems, such as Sn- and SnO 2 nanodots embedded in a holey carbon matrix. This work presents a new scalable methodology to confine/remold nanostructured materials in a carbon matrix which allows for the future design of functional materials with tunable composition and architecture.

Disciplines

Engineering | Physical Sciences and Mathematics

Publication Details

Wu, Z., Johannessen, B., Zhang, W., Pang, W., Mao, J., Liu, H. Kun. & Guo, Z. (2019). In situ incorporation of nanostructured antimony in an N-doped carbon matrix for advanced sodium-ion batteries. Journal of Materials Chemistry A, 7 (20), 12842-12850.

Authors

Zhibin Wu, Bernt Johannessen, Wenchao Zhang, Wei Kong Pang, Jianfeng Mao, Hua-Kun Liu, and Zaiping Guo

Title Page

Title

In-situ Incorporation of Nanostructured Antimony in N-doped Carbon Matrix for Advanced Sodium-Ion Batteries

Author names and affiliations

Zhibin Wu[ab], Bernt Johannessen[c], Wenchao Zhang[a], Wei Kong Pang[a], Jianfeng Mao[a], Hua Kun Liu[a], Zaiping Guo[ab*]

[a]Institute for Superconducting & Electronic Materials, University of Wollongong, Wollongong, NSW 2522, Australia

[b]School of Mechanical, Materials, Mechatronic and Biomedical Engineering, University of Wollongong, Wollongong, NSW 2522, Australia

[c]Australian Synchrotron, 800 Blackburn Rd, Clayton, VIC 3168, Australia

Corresponding Author

Zaiping Guo

Distinguished Professor, Australian Research Council (ARC) Future Fellow (FT3)

Associate Editor, ACS Applied Materials & Interfaces

School of Mechanical, Materials, Mechatronic, and Biomedical Engineering

Institute for Superconducting & Electronic Materials

Faculty of Engineering & Information Sciences

University of Wollongong, NSW 2522

T + 61 2 4221 5225

F + 61 2 4221 5731

E-mail: zguo@uow.edu.au

Keywords

Antimony; Sodium-ion Battery; Solvent-free; Embedding; Remolding

Abstract

Herein, a facile one-step and solvent-free pyrolysis method was developed to control the synthesis of nanostructured Sb embedded in an N-doped carbon matrix (Sb@G_xN_y-T, where *T*, G_x and N_y denotes the annealing temperature, the mass (*g*) of glucose and NH_4Cl used in the process, respectively). By adjusting these parameters, hybrid architectures can be *in-situ* constructed, including hollow Sb embedded in holeless carbon matrixes (Sb@$G_{0.25}N_{0.5}$-950) and Sb nanoplates embedded in holey carbon matrixes (Sb@$G_{0.25}N_{0.25}$-950). Our findings suggest that the formation of diverse nanostructures closely relate to the sublimation and evaporation of Sb, and the structural remold of liquid Sb by surface tension. Benefitting from the unique structural features, these optimized electrodes show highly reversible sodium storage with high specific capacities and good cycling stability. More importantly, it can be further extended to other material systems, such as Sn- and SnO_2 nanodots embedded in a holey carbon matrix. This work presents a new scalable methodology to confine/remold nanostructured materials in carbon matrix which allows for the future design of functional materials with tunable composition and architecture.

Introduction

Exploring new methods and theories to construct hybrid nanostructures is of great importance in current nanoscience. Complex micro-/nanostructures, based on an in-depth understanding of the formation mechanism of the functional composite materials, can significantly promote technological development in the energy storage/conversion, catalysis, and sensing fields to name a few[1-6]. Despite of the satisfactory advancement in constructing hybrid nanostructures, most approaches rely on complex solvent-based multistep reactions through engineering the given structure[7-10], which remains a challenge both practically and technically, thereby low-cost, highly-efficient and large-scale methods for hybrid material synthesis are urgently needed, especially for large-scale energy storage. Take Sn/C composite for example, metallic Sn nanosheets confined in graphene was reported for high-efficiency carbon dioxide electroreduction, but it includes multistep procedures involving chemical synthesis of ultrathin SnO_2 layers, coating SnO_2 with amorphous carbon by a hydrothermal method, and a thermal reduction process by calcination[9].

In addition, it is reported that antimony (Sb) can be utilised as a promising anode in sodium-ion batteries (SIBs) with a high theoretical capacity of 660 mAh g^{-1} and appropriate discharge voltage plateau (0.3-0.8 V vs. Na^+/Na)[11, 12]. However, a large volume expansion (293 %) upon complete sodiation to Na_3Sb leads to electrode pulverization and loss of contact with the current collector, ultimately resulting in rapid capacity fading, which clearly limits practical applications[13, 14]. To address these issues, various strategies have been developed to improve the electrochemical performance of

Sb-based materials either by tuning the morphologies and structures at the nanoscale or utilizing other materials as the buffer framework/layer[15-17]. For instance, Sb/C coaxial nanotubes were successfully prepared with a three-step method, involving hydrothermal synthesis of Sb_2S_3 nanorods, coating of polydopamine (PDA) on Sb_2S_3, and finally thermal reduction of Sb_2S_3/PDA at 500 °C. The optimized Sb/C electrode exhibits a capacity of 407 mAh g^{-1} after 240 cycles at 0.1 A g^{-1} in SIBs[18]. Another method for producing porous hollow Sb microspheres (prepared using Zn microspheres as templates and hydrochloric acid as an etching agent) resulted in a material with a reversible capacity of 617 mAh g^{-1} and capacity retention of 97.2 % after 100 cycles in SIBs[19]. However, such methods are not only time-consuming, but crucially difficult to control involving multiple and complex steps. Recently, general methods such as hydrothermal[2, 20] and chemical vapor deposition[21] have been intensively investigated for applications in nanomaterial synthesis with intriguing mechanisms presented, but there is sparse literature reporting the morphological evolution/mechanism of hybrid materials prepared by pyrolysis strategies under high temperature, especially when the temperature is elevated beyond its metallic melting point[22].

In the present work, we developed a facile and cost-effective pyrolysis strategy to fabricate Sb/C composite materials with tunable architectures through a one-step annealing treatment of a solid mixture consisting of $Sb(Ac)_3$, glucose and NH_4Cl. Both the annealing temperature and relative fraction of materials will alter the nanostructure morphology. For example, the architectures of Sb/C composite can change from a disordered morphology to a uniform matrix by increasing the annealing temperature,

and the thickness of carbon layers can be adjusted by the amount of glucose, whereas the NH_4Cl content can change the structures of Sb and carbon matrix. When these Sb/C composites were used as anodes for SIBs, they demonstrate different cycling stability for sodium storage due to their compositional and morphological differences. Furthermore, we also extended this synthetic strategy to other material systems, such as Sn- and SnO_2 nanodots embedded in a holey carbon matrix.

Experimental section

Synthesis of Sb/C composite

All the reagents used in the present study were purchased from Sigma-Aldrich. In a typical experiment, 2.0 g antimony acetate ($Sb(Ac)_3$), 0.25 g glucose and 0.25 g NH_4Cl (G/N = 0.25/0.25, G denotes the weight of glucose, and N denotes the weight of NH_4Cl, and $Sb(Ac)_3$ is fixed at 2.0 g) were manually mixed and ground for 30 min in an agate mortar, then the well-mixed powder was put in a capped crucible (semi-closed system) and heated at 950 ℃ for 2 h with a heating rate of 5 ℃ min^{-1} under Ar atmosphere in a tube furnace. After naturally cooling down, a black product with metallic color, marked as Sb@$G_{0.25}N_{0.25}$-950, was collected.

To evaluate the influence of calcination temperature, the well-mixed powder (G/N=0.25/0.25) was annealed at 450, 700 and 950 °C for 2 h with a heating rate of 5 ℃ min^{-1} under Ar atmosphere, and these obtained products were marked as Sb@$G_{0.25}N_{0.25}$-450, Sb@$G_{0.25}N_{0.25}$-700 and Sb@$G_{0.25}N_{0.25}$-950, respectively.

To evaluate the effect of NH_4Cl on morphology, 2.0 g $Sb(Ac)_3$ were respectively mixed with glucose and NH_4Cl in weight ratios of G/N=0.25/0.25, G/N=0.25/0.5 and

G/N=0.25/1.0. Then, they were annealed at 950 °C for 2 h under Ar atmosphere, and these obtained products were marked as Sb@$G_{0.25}N_{0.25}$-950, Sb@$G_{0.25}N_{0.5}$-950 and Sb@$G_{0.25}N_{1.0}$-950, respectively.

In addition, the influence of glucose on nanostructures was also studied. The well-mixed powder with weight ratios of G/N=0.125/0.5, G/N=0.25/0.5 and G/N=0.5/0.5 was annealed at 950 °C under Ar atmosphere, respectively, and these collected products were marked as Sb@$G_{0.125}N_{0.5}$-950, Sb@$G_{0.25}N_{0.5}$-950 and Sb@$G_{0.5}N_{0.5}$-950, respectively.

Synthesis of Sb from $Sb(Ac)_3$

Typically, 2.0 g $Sb(Ac)_3$ was heated at 450 ℃ with a heating rate of 5 ℃ min^{-1} for 2 h under Ar atmosphere in a tube furnace. Then, a silver-gray powder was collected directly without further treatment.

Other samples were respectively prepared at 150℃, 250℃, 350℃ and 700℃ following the same procedure.

Synthesis of SnO_2/C composite

0.8 g tin acetate ($Sn(Ac)_2$), 0.25 g glucose and 0.25 g NH_4Cl were manually mixed and ground for 30 min, then the well-mixed powder was heated at 450 ℃ with a heating rate of 5 ℃ min^{-1} for 2 h under Ar atmosphere in a tube furnace. After naturally cooling down, SnO_2/C composite was obtained without further treatment.

Synthesis of Sn/C composite

0.8 g tin acetate ($Sn(Ac)_2$), 0.25 g glucose and 0.25 g NH_4Cl were manually mixed and ground for 30 min, then the well-mixed powder was heated at 700 ℃ with a heating rate of 5 ℃ min^{-1} for 2 h under Ar atmosphere in a tube furnace. After naturally cooling

down, Sn/C composite was obtained without further treatment.

Characterization

The phase was identified by X-ray diffraction (XRD; MMA GBC) with a Cu K_α X-ray source at a scan rate of 2° min^{-1}. The morphologies and nanostructures of these obtained samples were observed by field emission scanning electron microscopy (FESEM; JEOL-7500) and transmission electron microscopy (TEM; JEOL-2010). Thermogravimetric analysis (TGA) was measured on a SETARAM thermogravimetric analyzer (France) in Ar or air atmosphere with a ramp rate of 5 ℃ min^{-1}. X-ray photoelectron spectroscopy (XPS) was collected by a VG Multilab 2000. Raman spectra were collected from a JOBIN Yvon Horiba Raman spectrometer model HR800 with a 10 mW helium/neon laser at 632.8 nm excitation. Synchrotron X-ray absorption spectroscopy (XAS) measurements were conducted at the wiggler XAS Beamline (12ID) at the Australian Synchrotron in Melbourne, Australia by using a set of liquid nitrogen cooled Si (311) monochromator crystals. The measurements were performed at the Sb K-edge (30.49 keV) in beamline Mode 3 in Hutch B. The data reduction follows standard methods using the ATHENA software package.

Electrochemical Measurement

The electrode was made by mixing the active material with super P and carboxymethyl cellulose (CMC) in a weight ratio of 80:10:10 in deionized water. The resultant slurries were then coated on copper foil and dried in a vacuum oven at 80 °C overnight, followed by pressing at 30 MPa. The mass loading of active material is ~1 mg cm^{-2}. CR2032 coin cells of SIBs were assembled in an argon-filled glove box, with metallic

Na foil served as both counter and reference electrode, glass microfiber served as the separator, and a mixture of 1.0 mol L^{-1} $NaClO_4$ in an ethylene carbonate (EC) / propylene carbonate (PC) solution (1:1, v/v) with 5 wt % addition of fluoroethylene carbonate (FEC) served as electrolyte.

These cells were assembled inside an argon-filled glove box (O_2 and H_2O level <0.1 ppm). The performance of each cell above was tested in the voltage range from 0.01 to 2.0 V with a Land battery-testing system at 25 °C. Cyclic voltammetry (CV) test was conducted in the voltage range between 0.01 to 2.0 V at 0.1 mV s^{-1} on a Biologic VPM3 electrochemical workstation.

Results and Discussion

Synthesis and structural analysis

The Sb/C composite material was prepared by a facile one-step annealing treatment of the solid mixture of $Sb(Ac)_3$, glucose and NH_4Cl. The formation process of embedding nanostructured Sb into the carbon matrix is illustrated in **Scheme 1**. By conjugating antimony oxychlorides ($Sb_4O_5Cl_2$) into two-dimensional (2D) carbon sheets, coupled with the reduction of Sb_2O_3 (decomposed from $Sb_4O_5Cl_2$) to Sb, followed by partial sublimation and evaporation of the extra Sb, Sb was eventually well-encapsulated in the carbon matrix with increased annealing temperature. The carbon matrix formed from the gradual polymerized molten syrup being carbonized into ultrathin carbon sheets at elevated temperatures, whereas chemically released gases generated from NH_4Cl blew glucose-derived polymers (such as melanoidin) into interconnected large

three-dimensional (3D) bubbles[23].

When only $Sb(Ac)_3$ was pyrolyzed, the chemical reaction process can be described by equation (1) and (4). As identified by ex-situ X-ray diffraction (XRD) (**Figure S1**), it firstly decomposed into cubic Sb_2O_3 and orthorhombic Sb_2O_3 at 150 ℃, and then the cubic phase gradually converted into an orthorhombic phase as the temperature increased. Above 450℃, Sb was obtained as Sb_2O_3 was reduced by carbon, and the generation of carbonaceous material was detected by Raman Spectroscopy (**Figure S2**). The thermal decomposition behavior of $Sb(Ac)_3$ was further measured by Thermogravimetric analysis (TGA), as displayed in **Figure 1b**. $Sb(Ac)_3$ is seen to loose mass consistent with the release of H_2O gas when heated from 140 ℃ to 240 ℃, resulting with the generation of intermediated phase of Sb_2O_3 and carbonaceous materials. The mass decreases only slowly from 430 ℃ to 500 ℃, corresponding to the reduction process from Sb_2O_3 to Sb. A further sharp drop from 530℃ to 630℃ can be ascribed to the sublimation of solid Sb. After that, the mass loss rate decreases since the solid Sb becomes liquid and was probably absorbed by the carbon matrix.

The pyrolysis products of the solid mixture (G/N= 0.25/0.25, G denotes the mass of glucose, and N denotes the mass of NH_4Cl) at different temperature stages were identified by XRD (**Figure 1a and Figure S3**), TGA (**Figure 1b**), Raman Spectroscopy (**Figure 1c**), and X-ray photoelectron spectroscopy (XPS) (**Figure 1d**). As described in **Figure 1a**, the solid mixture reveals a pyrolysis process which is different to $Sb(Ac)_3$. The ex-situ XRD patterns show that the mixture initially converted into $Sb_4O_5Cl_2$ at 150 ℃ whilst NH_4Cl did not fully decompose until 300 ℃. After that, Sb_2O_3 was

obtained when $Sb_4O_5Cl_2$ thermally decomposed into Sb_2O_3 and volatile $SbCl_3$. Above 450 ℃, Sb/C composite was obtained by reducing Sb_2O_3. Therefore, the main formation process of Sb could be described by the following chemical reaction equations (1-4)[24],

$$2Sb(CH_3COO)_3 \xrightarrow[\Delta]{} Sb_2O_3 + 12C + 9H_2O \uparrow \quad (1)$$

$$2Sb_2O_3 + 2HCl \xrightarrow[\Delta]{} Sb_4O_5Cl_2 + H_2O \uparrow \quad (2)$$

$$3Sb_4O_5Cl_2 \xrightarrow[\Delta]{} 5Sb_2O_3 + 2SbCl_3 \uparrow \quad (3)$$

$$Sb_2O_3 + 3C \xrightarrow[\Delta]{} 2Sb + 3CO \uparrow \quad (4)$$

From the TGA curve in **Figure 1b**, we can see that commercial pure Sb starts to sublimate at about 500 ℃, below its melting point of 630 ℃ in Ar atmosphere, and it evaporates continually also after melting. Besides, the solid mixture (G/N=0.25/0.25) displays a different mass loss trend to that of $Sb(Ac)_3$, showing a sharp mass loss between 150 and 220℃ due to the release of H_2O, NH_3, HCl and carbon oxides from NH_4Cl, $Sb(Ac)_3$ and glucose, together with a linear decrease between 220 and 530 ℃ due to the decomposition of intermediate phases, and an accelerated decrease after 530 ℃ due to the sublimation and evaporation of Sb. It was reported that the match between NH_4Cl salt decomposition (200-300℃) and glucose polymerization (200- 350 ℃) facilitates to produce the high-quality 3D sugar-blowing graphene[23]. In this work, the decomposition temperature of $Sb(Ac)_3$ (150-230℃) also matches well with that of NH_4Cl and glucose, and the mixture shows a sharp mass loss around 200 ℃, which could be advantageous to embed the intermediate phase into the carbon matrix synchronously by virtue of the bubble produced by the sugar-blowing process. The

carbon contents of the Sb/C composite prepared at 450, 700 and 950 ℃ were respectively calculated to be 23.7 %, 28.2 % and 31.4 % by analyzing the TGA curve in **Figure S4a**. The structural and electronic information of the Sb/C sample obtained at 450, 700 and 950 ℃ were further identified by Raman spectra. The G band can be ascribed to the in-plane bond-stretching motions of the graphitic sp^2-bonded carbon atoms and its position can be used to judge the disorder part of distorted hexagonal rings and chains[25], whilst the D band is linked to the out-plane vibrations from disordered sp^3 carbon atoms[26]. As was shown in **Figure 1c** that the Sb/C composite at 950 ℃ displays a D band peak at 1330 cm^{-1} and G band peak at 1589 cm^{-1} with the I_D/I_G ratio of 1.27, demonstrating that the carbonaceous material has an amorphous and defect-rich carbon structure. The decreasing value of I_D/I_G ratio further indicate the disordered carbon structure was converting more ordered with increasing carbonization temperature, which should be favorable for acquiring better electronic conduction. With the increasing of annealing temperature, the D band downshifted while the G-band upshifted, which means that the content of nitrogen which was doped in the carbon was decreasing[27]. The doping of nitrogen in carbon was then verified by the following XPS test. As we all known, XPS is an effective tool to survey the chemical state and surface composition of the Sb/C composite. In the full-survey-scan XPS spectrum (**Figure S4b**), the characteristic peaks of Sb, C, O and N are observed, demonstrating the coexistence of these elements in the composite. The N1s spectrum in **Figure 1d** at 950 ℃ can be separated into three different peaks at 399.0, 401.6, and 402.7 eV, which can be assigned to pyridinic N, quaternary N, and oxidized N, respectively[28]. The N1s spectrums at 450℃

and 700 ℃ can be separated into three individual peaks at 399.0, 401.6 eV and 400.6 eV, which can be assigned to pyridinic N, quaternary N and pyrrolic N, respectively. With the increasing of annealing temperature, the content of pyridinc N decreased while the content of quaternary N increased, and oxidized N suddenly appeared at 950℃, due to the different thermodynamics stability of the nitrogen functional group.[29] These results demonstrate that the amorphous carbon structure was doped by nitrogen atoms within the five or six-membered aromatic rings. The amorphous carbon structures doped by nitrogen are believed to facilitate electron transfer and sodium-ion diffusion kinetics for improving battery performance[30].

To survey the effect of NH_4Cl, glucose and temperature on the morphological evolution of Sb/C composite, field emission scanning electron microscopy (FESEM) and transmission electron microscopy (TEM) tests were conducted. The glucose and NH_4Cl can provide a three-dimensional carbon sheets bubble[23] (**Figure S5**) via a sugar-blowing strategy for the growth of the synchronously generated Sb-based intermediate phases. By increasing the annealing temperature from 450 ℃ (**Figure 2a-c**) to 700 ℃ (**Figure 2j-l**), the Sb particles anchored on the carbon matrix sublimated, then Sb nanoparticles that were uniformly embedded in the carbon matrix were retained.[18] The elemental mapping of Sb@$G_{0.25}N_{0.25}$-450 (**Figure 2d-g**) clearly evident that these larger Sb microparticles were randomly anchored on the carbon matrix. The TEM images of Sb@$G_{0.25}N_{0.25}$-450 **(Figure 2h and i)** reveal that parts of Sb nanoparticles (ca. 200 nm) have been embedded in the matrix at this temperature. When further increased to 950℃ (**Figure 2m-o**), Sb embedded in the carbon matrix further evaporated, thereby Sb

nanoplates with smaller size (ca. 100 nm) were remolded in the carbon matrix when it cooled down. In addition to investigating the morphological evolution of the solid mixture (G/N=0.25/0.25), we also studied the morphological evolution of the solid mixture (G/N=0.25/0.5) with a variety of annealing temperatures (**Figure S6**), which demonstrates consistent conclusions that the morphological transitions from disordered to ordered were dominated by sublimation while the structural changes of the embedded Sb were dominated by evaporation and remolding.

By adjusting the amount of NH_4Cl, the structure of Sb and carbon matrix can be adjusted, as shown in **Figure 3**. Deducing from the released gas (such as NH_3 and HCl), interconnected holey carbon matrix embedded with Sb nanoplates (Sb@$G_{0.25}N_{0.25}$-950) was obtained when 0.25 g NH_4Cl was added, along with $Sb_4O_5Cl_2$ and Sb_2O_3 serving as intermediate precursors. In this system, NH_4Cl not only functioned as gas sources but also acted as an acid source to generate oxychlorides by reacting with Sb_2O_3. Surprisingly, with further increased amount of NH_4Cl, the nanostructure of Sb became semienclosed hollow bowls while interconnected holey carbon matrix turned into matrix with tiny scattered holes. Since increased HCl and NH_3 gases release could help build bigger caves for encapsulating Sb and also provide larger bubble template for the growth of larger-area carbon sheet, the *in-situ* embedded Sb occupying these caves would then remold into bowl-like Sb when cooled down, imprinting from the curved liquid surface and following the shape of the caves. When the amount of NH_4Cl increased to 1 g, tiny holes in the carbon matrix nearly disappeared and the nanostructure of Sb recovered to nanosheet again. It turns out that NH_4Cl can be

effective to modify the porosity of the carbon matrix as well as change the nanostructure of Sb. Notably, the high temperature, stimulating the continuously sublimation and evaporation of Sb, was also critical important to create extra spaces for remolding unique Sb nanostructures. The morphological formation mechanism is different with the report from Lou's group[18], since they tuned the hollow structures of their Sb/C coaxial nanotubes at 500℃ with different annealing time by virtue of the partial sublimation of Sb within the nanotube. Their annealing temperature is lower than the melting point of 631℃ but located at the sublimation point of metallic Sb. In our work, the annealing temperature is higher than the melting point and the Sb remains liquid state at 950℃, which brings new sights on tuning nanostructures via nano-remolding.

By changing the amount of glucose merely, the thickness of carbon layers was controlled, as shown in **Figure S7**. It is clearly observed that the thickness of carbon layers is in direct proportion to the adding amount of glucose, and the hollow structure of Sb and carbon matrix were well-maintained with 0.5 g NH_4Cl added.

In addition to embedding nanostructured Sb into carbon matrix shown above, this strategy can be also applied to embed Sn nanodots and SnO_2 nanodots into the 2D holey carbon matrix, as shown in **Figure S8**.

Sodium-ions Storage

The sodium storage property of Sb@$G_{0.25}N_{0.25}$-950 electrode was studied by cyclic voltammetry (CV) at 0.1 mV s^{-1} with a potential window between 0.01 and 2 V (**Figure 4a**). During the first cathodic sweep, it shows one broad reduction peak at 0.33 V, which can be assigned to the formation of solid electrolyte interface (SEI) layers and the

alloying reactions between Sb and Na. During the first anodic sweep, the electrode shows a single oxidation peak at 0.89 V due to the extraction of Na from Na_3Sb. In the subsequent cathodic sweep, it shows three reduction peaks, indicating multiply steps of alloying process involving several intermediate phases ($Sb + xNa^+ + xe^- \rightarrow Na_xSb$, $x \leqslant 3$)[31]. The rate performances of the Sb@$G_{0.25}N_{0.25}$-450, Sb@$G_{0.25}N_{0.25}$-700 and Sb@$G_{0.25}N_{0.25}$-950 for SIBs were compared with various current densities ranging from 0.1 to 2 A g^{-1} (**Figure 4b**). The Sb@$G_{0.25}N_{0.25}$-950 electrode shows the best rate performance, delivering high capacities of 485, 461, 436, 415 and 351 mAh g^{-1} at 0.1, 0.2, 0.5, 1 and 2 A g^{-1}, respectively (**Figure 4c**). More importantly, its capacity can even recover to ca. 470 mA g^{-1} when the current density returns to 0.1 mA g^{-1}, demonstrating its excellent rate capability. By contrast, the Sb@$G_{0.25}N_{0.25}$-450 electrode displays inferior rate performance, retaining capacity of only ca. 240 mA h g^{-1} when the current density increases to 2 A g^{-1} and recovering to merely ca. 390 mA h g^{-1} at 0.1 A g^{-1}, although it displays the highest capacity of ca. 510 mA g^{-1} at 0.1 A g^{-1} at the very beginning. The cycling performances of these electrodes were tested at the current density of 0.1 A g^{-1} over a potential window between 0.01 and 2 V in SIBs. As shown in **Figure 4d**, the Sb@$G_{0.25}N_{0.25}$-950 electrode shows the best cycling stability with capacity retention rate of 87.4 %, maintaining as high as 419 mAh g^{-1} after 100 cycles, whilst Sb@$G_{0.25}N_{0.25}$-450 electrode shows the lowest capacity retention rate of 77.1 % after 100 cycles. It turns out that the structural transitions from disordered structure to ordered matrix tuned by annealing temperature facilitates to acquire better cycling stability and rate capability.

Furthermore, we also evaluated the cycling stability of these electrodes prepared by different amount of NH_4Cl and glucose, as shown in **Figure 4e and f.** Obviously, the cycling stability of these electrodes (prepared with NH_4Cl) for SIBs is better than that of the $Sb@G_{0.25}$-950 electrode (prepared without NH_4Cl). Among them, bowl-like $Sb@G_{0.25}N_{0.5}$-950 electrode shows the best cycling stability, maintaining 352 mAh g^{-1} after 100 cycles with capacity retention of 91.7 %, while holey $Sb@G_{0.25}N_{0.25}$-950 electrode maintains 419 mAh g^{-1} after 100 cycles with capacity retention of 87.4 %. It is noted that the bowl-like Sb are favorable to provide extra space to relieve the volume expansion during alloying-dealloying process, while the holey carbon N-doped matrix facilitates to shorten ion/electron transport path[19]. With the increasing of carbon content by adding more glucose (**Figure 4f**), the cycling stability becomes better since thicker carbon layers can provide much stronger buffer layers to alleviate the large volume changes from Sb. Remarkably, the $Sb@G_{0.5}N_{0.5}$-950 can achieve high capacity retention of 94.4 % after 100 cycles despite of its low capacity of 331 mAh g^{-1}.

To investigate the electrode reaction process, ex-situ X-ray absorption spectroscopy (XAS) was conducted. The discharge-charge voltage profiles for the first one and a half cycles of the $Sb@G_{0.25}N_{0.25}$-950 electrode are given in **Figure 4g**, with six marked points at the voltage profile for the XAS study. Upon sodiation **(Figure 4h)**, the Sb K-edge shifts negligibly, owing to the very short core-hole lifetime at the Sb K-edge (30.49 KeV), which leads to a poor energy resolution, and the overall shape varies very slightly only and with broad features[32]. The intensity of the white line decreases gradually for the normalized data, which results from the decrease of the unoccupied p states (Na^+

alloyed with Sb during discharging)[33]. The Fourier transformed (FT) extended X-ray absorption fine structure (EXAFS) in the inset shows that the peak of the initial electrode (D 2 V) at 1.3 Å (Sb-O bond) disappeared after full discharge. The Sb-O bond could come from the carboxymethyl cellulose binder chemically bonded to metallic Sb since the Sb-O bond was not observed in the Sb@$G_{0.25}N_{0.25}$-950 powder (**Figure S9**), which is helpful to build robust electrode structures [34, 35]. Importantly, the Sb-O bond in this electrode is reversible (**Figure 4i**) as it restores to its initial state when fully charged (DC 2 V), which facilitates to harvest stable cycling performance. However, the first Na-Sb and Sb-Sb coordination shells show a very close bond distances, making it very hard to distinguish and simulate the intermediate phases[36].

Conclusion

In summary, a facile one-step and scalable pyrolysis strategy was developed to control the synthesis of Sb/C composite materials with nanostructured Sb and N-doped carbon matrix. By adjusting the annealing temperature, the amount of NH_4Cl and/or glucose used in the process, novel architectures such as bowl-like hollow Sb or Sb nanoplates embedded in the carbon matrix were obtained. Our findings suggests that the formation of diverse Sb/C composite material should be closely related to the sublimation and evaporation of Sb at high temperature, the structural remold of liquid Sb within NH_4Cl-glucose-derived carbon sheets by surface tension. The electrochemical performance of these composite electrodes investigated as anodes for SIBs were compared and discussed, and the optimized holey Sb@$G_{0.25}N_{0.25}$-950 electrode shows both cycling

stability and high capacity, benefiting from the holey architecture that facilitates to address the restacking and accommodate the volume expansion of Sb. Besides, this one-step synthetic procedure can be extended to prepare other material systems and it also provides new insights and practical methods for designing tunable composite architectures and composition for catalyst and sensor applications.

Acknowledgements

Financial support from the Australian Research Council (ARC) (FT150100109, FT160100251, and DP170102406) is gratefully acknowledged. The authors also would like to thank AINSE Ltd for providing financial assistance (Award - PGRA). Part of this research was undertaken on the XAS beamline at the Australian Synchrotron, part of ANSTO. The authors thank the Electron Microscopy Centre (EMC) at the University of Wollongong for the electron microscopy characterizations.

Reference

1. P. G. Bruce, B. Scrosati and J. M. Tarascon, *Angew. Chem. Int. Ed.*, 2008, **47**, 2930-2946.
2. L. Yu, X. Y. Yu and X. W. Lou, *Adv. Mater.*, 2018, **30**, 1800939.
3. L. Li, Y. Zheng, S. Zhang, J. Yang, Z. Shao and Z. Guo, *Energy Environ. Sci.*, 2018, **11**, 2310-2340.
4. H. Hou, C. E. Banks, M. Jing, Y. Zhang and X. Ji, *Adv. Mater.*, 2015, **27**, 7861-7866.
5. S. Zhang, Y. Zheng, X. Huang, J. Hong, B. Cao, J. Hao, Q. Fan, T. Zhou and Z. Guo, *Adv. Energy Mater.*, 2019, 1900081.
6. Y. Fang, X. Y. Yu and X. W. Lou, *Angew. Chem. Int. Ed.*, 2017, **56**, 5801-5805.
7. H.-H. Li, L. Zhou, L.-L. Zhang, C.-Y. Fan, H.-H. Fan, X.-L. Wu, H.-Z. Sun and J.-P. Zhang, *ACS Energy Lett.*, 2016, **2**, 52-59.
8. Y. Zhang, C. W. Foster, C. E. Banks, L. Shao, H. Hou, G. Zou, J. Chen, Z. Huang and X. Ji, *Adv. Mater.*, 2016, **28**, 9391-9399.
9. F. Lei, W. Liu, Y. Sun, J. Xu, K. Liu, L. Liang, T. Yao, B. Pan, S. Wei and Y. Xie, *Nat. Commun.*, 2016, **7**, 12697.
10. X. Y. Yu, L. Yu, L. Shen, X. Song, H. Chen and X. W. Lou, *Adv. Funct. Mater.*, 2014, **24**, 7440-7446.

11. J. Song, P. Yan, L. Luo, X. Qi, X. Rong, J. Zheng, B. Xiao, S. Feng, C. Wang and Y.-S. Hu, *Nano Energy*, 2017, **40**, 504-511.
12. M. He, K. Kravchyk, M. Walter and M. V. Kovalenko, *Nano Lett.*, 2014, **14**, 1255-1262.
13. V. Chevrier and G. Ceder, *J. Electrochem. Soc.*, 2011, **158**, A1011-A1014.
14. L. Wu, H. Lu, L. Xiao, X. Ai, H. Yang and Y. Cao, *J. Mater. Chem. A*, 2015, **3**, 5708-5713.
15. Y. Fang, X. Y. Yu and X. W. Lou, *Angew. Chem. Int. Ed.*, 2018, **57**, 9859-9863.
16. P. Li, X. Guo, S. Wang, R. Zang, X. Li, Z. Man, P. Li, S. Liu, Y. Wu and G. Wang, *J. Mater. Chem. A*, 2019, **7**, 2553-2559.
17. M. Deng, S. Li, W. Hong, Y. Jiang, W. Xu, H. Shuai, G. Zou, Y. Hu, H. Hou and W. Wang, *Mater. Chem. Phys.*, 2019, **223**, 46-52.
18. Z. Liu, X.-Y. Yu, X. W. D. Lou and U. Paik, *Energy Environ. Sci.*, 2016, **9**, 2314-2318.
19. H. Hou, M. Jing, Y. Yang, Y. Zhang, Y. Zhu, W. Song, X. Yang and X. Ji, *J. Mater. Chem. A*, 2015, **3**, 2971-2977.
20. L. Yu, H. Hu, H. B. Wu and X. W. Lou, *Adv. Mater.*, 2017, **29**, 1604563.
21. Y. Shi, H. Li and L.-J. Li, *Chem. Soc. Rev.*, 2015, **44**, 2744-2756.
22. M. Chhowalla, H. S. Shin, G. Eda, L.-J. Li, K. P. Loh and H. Zhang, *Nat. Chem.*, 2013, **5**, 263.
23. X. Wang, Y. Zhang, C. Zhi, X. Wang, D. Tang, Y. Xu, Q. Weng, X. Jiang, M. Mitome and D. Golberg, *Nat. Commun.*, 2013, **4**, 2905.
24. L. Costa, G. Paganetto, G. Bertelli and G. Camino, *J. Therm. Anal.*, 1990, **36**, 1141-1153.
25. K. Bogdanov, A. Fedorov, V. Osipov, T. Enoki, K. Takai, T. Hayashi, V. Ermakov, S. Moshkalev and A. Baranov, *Carbon*, 2014, **73**, 78-86.
26. A. C. Ferrari and J. Robertson, *Phys. Rev. B*, 2000, **61**, 14095.
27. Q.-H. Yang, P.-X. Hou, M. Unno, S. Yamauchi, R. Saito and T. Kyotani, *Nano Lett.*, 2005, **5**, 2465-2469.
28. H. Schmiers, J. Friebel, P. Streubel, R. Hesse and R. Köpsel, *Carbon*, 1999, **37**, 1965-1978.
29. Y. Yamada, Y. Suzuki, H. Yasuda, S. Uchizawa, K. Hirose-Takai, Y. Sato, K. Suenaga and S. Sato, *Carbon*, 2014, **75**, 81-94.
30. Y. Liu, N. Zhang, L. Jiao and J. Chen, *Adv. Mater.*, 2015, **27**, 6702-6707.
31. T. Wu, C. Zhang, H. Hou, P. Ge, G. Zou, W. Xu, S. Li, Z. Huang, T. Guo and M. Jing, *Adv. Funct. Mater.*, 2018, **28**, 1705744.
32. M. Fehse, A. Darwiche, M. T. Sougrati, E. M. Kelder, A. V. Chadwick, M. Alfredsson, L. Monconduit and L. Stievano, *Chem. Mater.*, 2017, **29**, 10446-10454.
33. D. Chen, C. Li, Z. Zhu, J. Fan and S. Wei, *Phys. Rev. B*, 2005, **72**, 075341.
34. Y. Liu, Z. Tai, T. Zhou, V. Sencadas, J. Zhang, L. Zhang, K. Konstantinov, Z. Guo and H. K. Liu, *Adv. Mater.*, 2017, **29**, 1703028.
35. Y. X. Wang, Y. Xu, Q. Meng, S. L. Chou, J. Ma, Y. M. Kang and H. K. Liu, *Adv. Mater. Interfaces*, 2016, **3**, 1600662.
36. L. Baggetto, K. J. Carroll, H.-Y. Hah, C. E. Johnson, D. R. Mullins, R. R. Unocic, J. A. Johnson, Y. S. Meng and G. M. Veith, *J. Phys. Chem. C*, 2014, **118**, 7856-7864.

Scheme 1 (a) Schematic illustration of the formation process of nanostructured Sb embedded in the carbon matrix.

Figure 1(a) XRD patterns of the solid mixture (G/N=0.25/0.25) annealed at 150, 300, 400 and 450 ℃, respectively. Notation: # represents the peaks of Sb_2O_3 while * represents the peaks of NH_4Cl in the figure (b) TGA curves of commercial Sb powder, $Sb(Ac)_3$, and the solid mixture (G/N=0.25/0.25) in Ar atmosphere (c) Raman spectra and (d) High-resolution N1s XPS patterns of Sb/C composite prepared at 450, 700 and 950 ℃, respectively.

Figure 2 SEM images of Sb/C composite prepared at different temperatures of 450, 700 and 950 ℃, corresponding to (a-c) Sb@$G_{0.25}N_{0.25}$-450, (j-l) Sb@$G_{0.25}N_{0.25}$-700 and (m-o) Sb@$G_{0.25}N_{0.25}$-950, respectively. (d) EDS spectrum, (e-g) EDS mappings and (h and i) TEM images of Sb@$G_{0.25}N_{0.25}$-450.

Figure 3 Morphological characterization of Sb/C composite prepared by different amount of NH_4Cl at 950℃. SEM images of (a-b) Sb@$G_{0.25}N_{0.25}$-950, (d-e) Sb@$G_{0.25}N_{0.5}$-950, (g-h) Sb@$G_{0.25}N_{1.0}$-950. TEM images of (c) Sb@$G_{0.25}N_{0.25}$-950, (f) Sb@$G_{0.25}N_{0.5}$-950, (i) Sb@$G_{0.25}N_{1.0}$-950. HRTEM image (inset) and SAED pattern (inset) of (c) Sb@$G_{0.25}N_{0.25}$-950.

Figure 4 (a) CV curves of Sb@$G_{0.25}N_{0.25}$-950 electrode measured at a sweep rate of 0.1 mV s^{-1} for SIBs, (b) Rate capability of Sb@$G_{0.25}N_{0.25}$-450, Sb@$G_{0.25}N_{0.25}$-700 and Sb@$G_{0.25}N_{0.25}$-950 electrodes at various current densities from 0.1 to 2 A g^{-1}. (c) Charge-discharge curves of Sb@$G_{0.25}N_{0.25}$-950 at various current densities from 0.1 to 2 A g^{-1}. (d-f) Cycling performance measured at 0.1 A g^{-1} with electrodes prepared by different annealing temperature, different amount of glucose and NH_4Cl, respectively. (g) Voltage vs. time profiles of Sb@$G_{0.25}N_{0.25}$-950 electrode for 1st and a half cycles. (h and i) Normalized absorption spectra and its corresponding Fourier transforms (inset) at the Sb K-edge of Sb@$G_{0.25}N_{0.25}$-950 electrodes with various states of charge. Notation: D stands for discharge and C stands for charge.

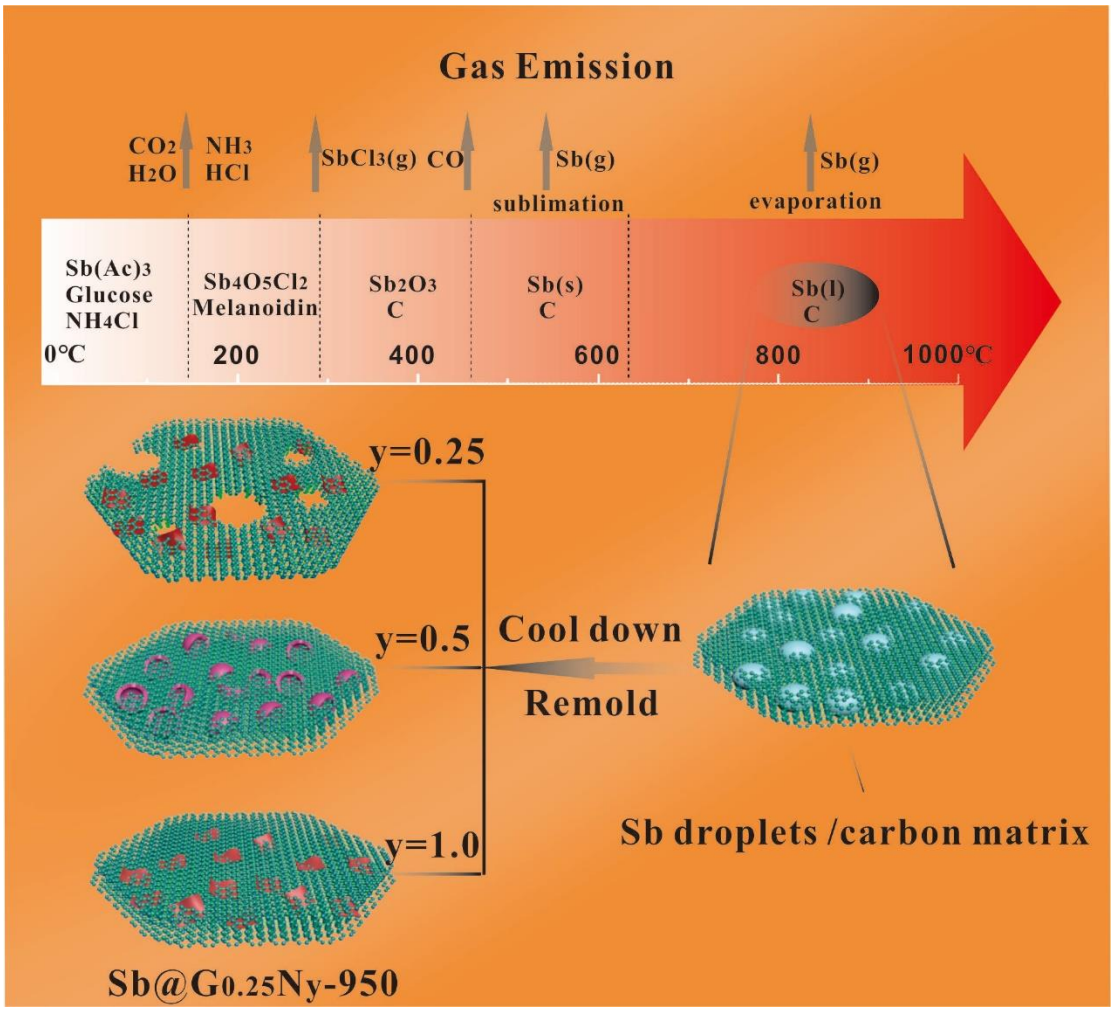

Scheme 1 (a) Schematic illustration of the formation process of nanostructured Sb embedded in the carbon matrix.

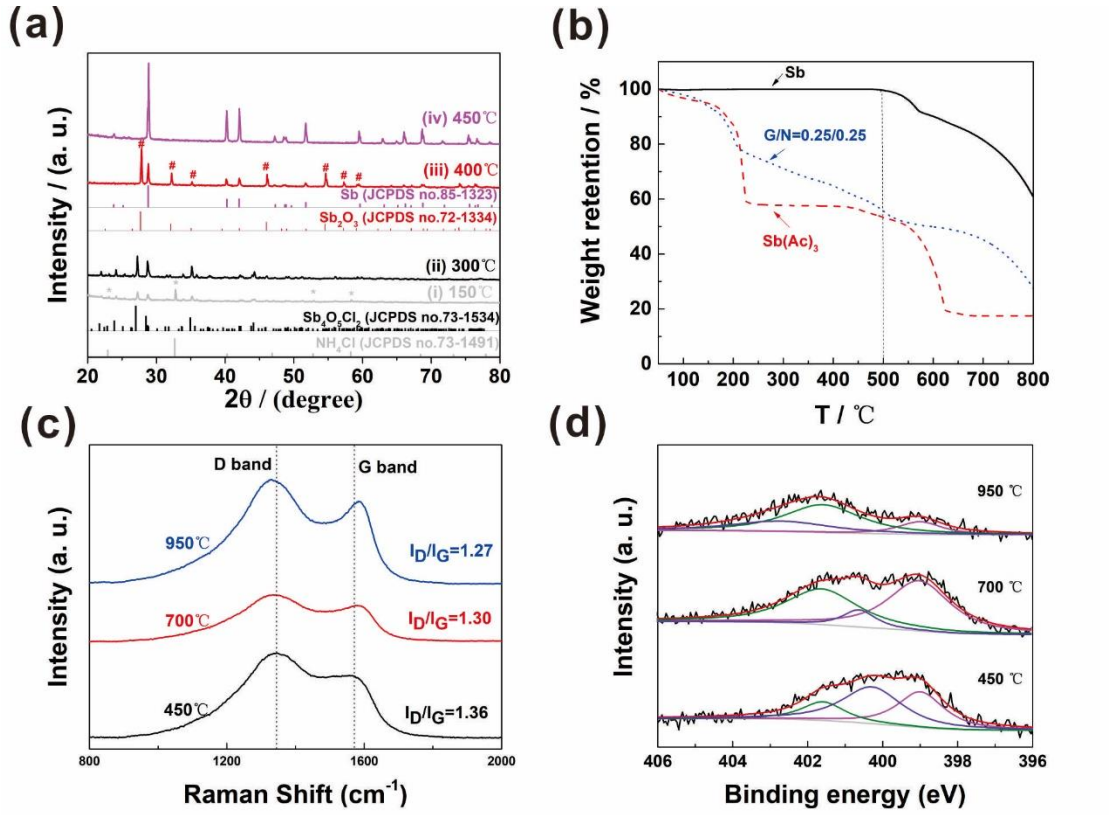

Figure 1(a) XRD patterns of the solid mixture (G/N=0.25/0.25) annealed at 150, 300, 400 and 450 ℃, respectively. Notation: # represents the peaks of Sb_2O_3 while * represents the peaks of NH_4Cl in the figure (b) TGA curves of commercial Sb powder, $Sb(Ac)_3$, and the solid mixture (G/N=0.25/0.25) in Ar atmosphere (c) Raman spectra and (d) High-resolution N1s XPS patterns of Sb/C composite prepared at 450, 700 and 950 ℃, respectively.

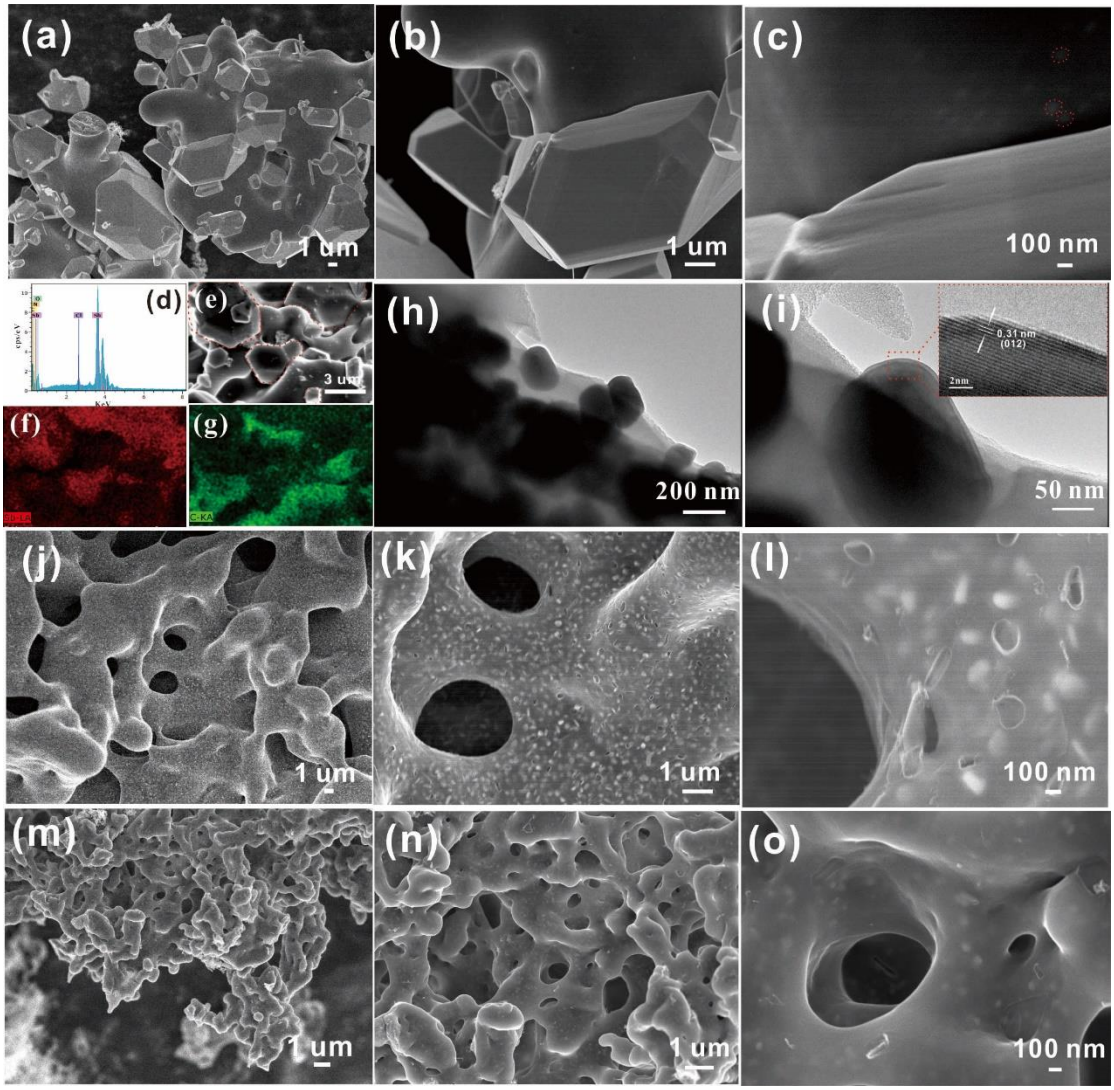

Figure 2 SEM images of Sb/C composite prepared at different temperatures of 450, 700 and 950 °C, corresponding to (a-c) Sb@$G_{0.25}N_{0.25}$-450, (j-l) Sb@$G_{0.25}N_{0.25}$-700 and (m-o) Sb@$G_{0.25}N_{0.25}$-950, respectively. (d) EDS spectrum, (e-g) EDS mappings and (h and i) TEM images of Sb@$G_{0.25}N_{0.25}$-450.

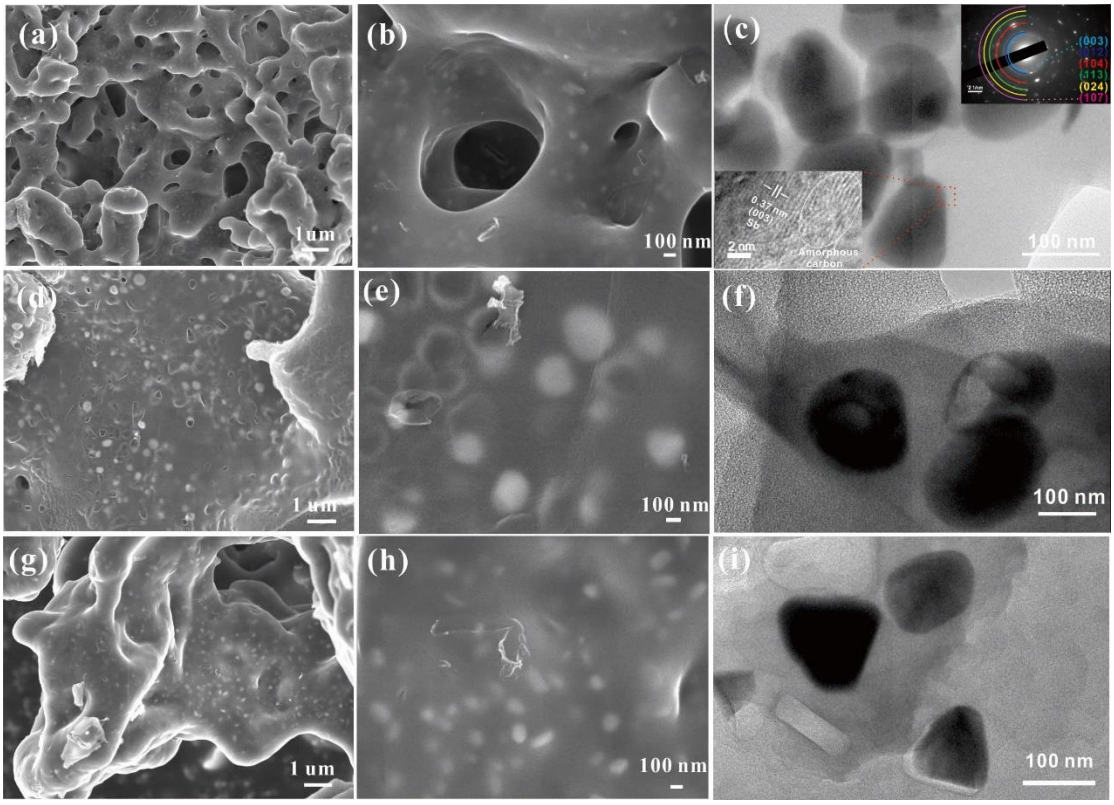

Figure 3 Morphological characterization of Sb/C composite prepared by different amount of NH_4Cl at 950℃. SEM images of (a-b) Sb@$G_{0.25}N_{0.25}$-950, (d-e) Sb@$G_{0.25}N_{0.5}$-950, (g-h) Sb@$G_{0.25}N_{1.0}$-950. TEM images of (c) Sb@$G_{0.25}N_{0.25}$-950, (f) Sb@$G_{0.25}N_{0.5}$-950, (i) Sb@$G_{0.25}N_{1.0}$-950. HRTEM image (inset) and SAED pattern (inset) of (c) Sb@$G_{0.25}N_{0.25}$-950.

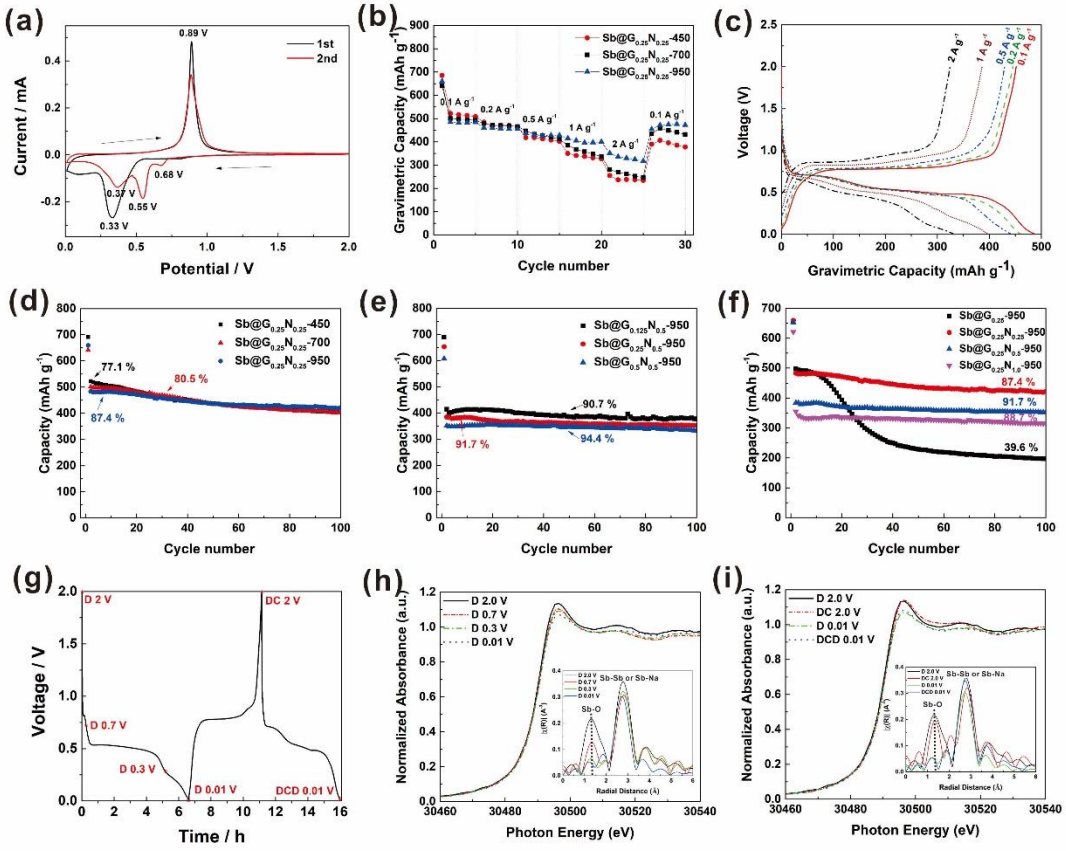

Figure 4 (a) CV curves of Sb@$G_{0.25}N_{0.25}$-950 electrode measured at a sweep rate of 0.1 mV s^{-1} for SIBs, (b) Rate capability of Sb@$G_{0.25}N_{0.25}$-450, Sb@$G_{0.25}N_{0.25}$-700 and Sb@$G_{0.25}N_{0.25}$-950 electrodes at various current densities from 0.1 to 2 A g^{-1}. (c) Charge-discharge curves of Sb@$G_{0.25}N_{0.25}$-950 at various current densities from 0.1 to 2 A g^{-1}. (d-f) Cycling performance measured at 0.1 A g^{-1} with electrodes prepared by different annealing temperature, different amount of glucose and NH_4Cl, respectively. (g) Voltage vs. time profiles of Sb@$G_{0.25}N_{0.25}$-950 electrode for 1st and a half cycles. (h and i) Normalized absorption spectra and its corresponding Fourier transforms (inset) at the Sb K-edge of Sb@$G_{0.25}N_{0.25}$-950 electrodes with various states of charge. Notation: D stands for discharge and C stands for charge.